RESEARCH ARTICLE

Inorganic-rich Solid Electrolyte Interphase for Advanced Lithium Metal Batteries in Carbonate Electrolytes

Sufu Liu,[a, +] Xiao Ji,[a,+] Nan Piao,[a,+] Ji Chen,[a] Nico Eidson,[a] Jijian Xu,[a] Pengfei Wang,[a] Long Chen,[a] Jiaxun Zhang,[a] Tao Deng,[a] Singyuk Hou,[a] Ting Jin,[a] Hongli Wan,[a] Jingru Li,[b] Jiangping Tu,[b] Chunsheng Wang [a,*]

[a] Department of Chemical and Biomolecular Engineering, University of Maryland, College Park, MD, 20740, United States

[b] State Key Laboratory of Silicon Materials, Key Laboratory of Advanced Materials and Applications for Batteries of Zhejiang Province, and School of Materials Science& Engineering, Zhejiang University, Hangzhou, 310027, China

* Corresponding Author: cswang@umd.edu

+ These authors contribute equally to this work.

Abstract: In carbonate electrolytes, the organic-inorganic solid electrolyte interphase (SEI) formed on the lithium (Li) metal anode surface is strongly bonded to Li and experiences the same volume change as Li, thus it undergoes continuous cracking/reformation during plating/stripping cycles. Here, an inorganic-rich SEI is designed on a Li metal surface to reduce its bonding energy with Li metal by dissolving 4 M concentrated $LiNO_3$ in dimethyl sulfoxide (DMSO) as an additive for a fluoroethylene carbonate (FEC) based electrolyte. Due to the aggregate structure of NO_3^- ions and its participation in the primary Li^+ solvation sheath, abundant Li_2O, Li_3N, and LiN_xO_y grains are formed in the resulting SEI, in addition to the uniform LiF distribution from the reduction of PF_6^- ions. The inorganic-rich SEI's weak bonding (high interface energy) to Li can effectively promote Li diffusion along the SEI/Li interface and prevent Li dendrite penetration into the SEI. As a result, our designed carbonate electrolyte enables a Li anode to achieve a high Li plating/stripping CE of 99.55% (1 mA cm^{-2}, 1.0 mAh cm^{-2}) and the electrolyte also enables a $Li||LiNi_{0.8}Co_{0.1}Mn_{0.1}O_2$ (NMC811) full cell (2.5 mAh cm-2) to retain 75% of its initial capacity after 200 cycles with an outstanding CE of 99.83%. The concentrated additive strategy presented here provides a drop-in practical solution to further optimize carbonate electrolytes for beyond Li-ion batteries.

Introduction

The ever-increasing demand for electric vehicles and portable electronics has revitalized the long-term pursuit of Li-ion batteries with higher energy density.[1-3] Due to having the most electronegative potential (-3.04 V vs. standard hydrogen electrode) and >10 times higher capacity (3860 mAh g^{-1}) than graphite anodes, Li metal anode batteries can potentially deliver a higher power and energy density, especially when it is coupled with the high-voltage and high-specific-capacity nickel-rich $LiNi_xCo_yMn_{1-x-y}O_2$ (Ni-rich NMC, Ni ≥ 60%) cathode [4-5]. However, the highly active Li metal reacts with electrolytes and often forms dendrites, resulting in a low Coulombic efficiency (CE) and fast capacity decay. The Li dendrite growth also raises safety hazards with short-circuit concerns, which severely limit the practical applications of rechargeable Li metal batteries (LMBs).[6-8]

Almost all organic electrolytes will be reduced on metallic Li. Once the Li metal is immersed in carbonate electrolytes, unavoidable reactions occur instantaneously [9-10], forming an organic-inorganic solid electrolyte interphase (SEI) [11-12] to prevent further reaction. However, the nonuniform organic-inorgansic SEI cannot dynamically bear the huge volume change during Li plating/stripping cycles, leading to the continuous SEI cracking/reformation, and even Li dendrite formation.[13-15] Therefore, a robust artificial SEI which can accommodate the large volume change of Li is necessary for high-performance LMBs.

To avoid the fracturing of the SEI, most researches focus on increasing the mechanical flexibility of the SEI to accommodate the infinite volume change during Li plating/stripping by increasing the organic-content in the SEI, and even forming a pure polymer SEI.[16-17] However, the strong bonding (lithiophilicity) between the organic SEI and Li metal also causes the SEI to suffer the same volume change as Li during Li plating/stripping [18-19], and the organic SEI cannot withstand the infinite volume change of the plated Li without breaking. Therefore, the cracking of the organic SEI is unavoidable, as evidenced by the reported low CE. Besides, the strong bonding of the organic SEI with Li also restricts the Li diffusion along the SEI/Li interface and promotes vertical Li penetration into the SEI to form Li dendrites. This dendritic growth is due to the lithiophlic nature and low interfacial energy of the SEI. Since inorganic lithium compounds (such as LiF, Li_2O, Li_3N, etc.) have weak bonding (lithiophobicity) with a high interfacial energy with Li metal [20-22], these ceramic SEIs can boost the Li lateral diffusion along the SEI/Li interface and suppress metallic Li from penetrating into the inorganic SEI. Meanwhile, the ceramic SEI with a high Young's modulus is also mechanically strong for better suppression of dendritic growth and penetration of the interface. Therefore, a uniform inorganic SEI with a lithiophobic property is desirable for an advanced Li metal anode, or at least an inorganic-rich layer closely attached to metallic Li is highly required.

The chemical composition of the SEI can be manipulated by tailoring the electrolyte composition, which can alter the interfacial electrolyte environment on electrodes. Among all organic electrolytes, carbonate electrolytes have been extensively used in commercial Li-ion batteries because the flexible organic-inorganic SEIs are strongly bonded to graphite and effectively accommodate the small volume change (~13%) of graphite during Li intercalation/deintercalation.[23] However, organic-inorganic SEIs cannot accommodate the volume change of a Li metal anode. A large number of additives have been explored in carbonate electrolytes to change the SEI composition. Among the additives, fluoroethylene carbonate (FEC) [24-25] and vinylene carbonate (VC) [26-27] are the most effective additives for carbonate electrolytes because they promote the formation of inorganic LiF and Li_2CO_3 components in the SEI. When used for Li/S batteries, the protective layer formed by FEC in carbonate-based electrolyte is also found to suppress the polysulfide attack against the metal Li anode.[28] However, the reduction of FEC and VC also produces

organic compounds, which weaken the effectiveness of FEC and VC for Li-dendrite-suppression.[29-30] Adding more inorganic salts (such as $LiPF_6$ and $LiNO_3$) into the electrolyte can increase the contact ion pair and aggregate solvates but it can also reduce the solvation separated ion pair, which will promote reduction of inorganic salts to form an inorganic-rich SEI. $LiNO_3$ has been regarded as one of the most successful SEI precursor in ether-based electrolytes especially for Li/S batteries, which can react with metallic Li to form a passivation layer and hence suppress redox shuttles of lithium polysulfide.[31-32] However, its poor solubility in both acyclic and cyclic carbonate solvents has long restrained its application in carbonate electrolytes. One method is to maintain $LiNO_3$ in carbonate solvents by implanting $LiNO_3$ particles into porous PVDF-HFP [29] or glass fiber [33] as separators or coating layers on Li metal anode surfaces, which will be continuously dissolved into the electrolyte when the trace amount of dissolved $LiNO_3$ in the electrolyte is consumed. Another method is to add $LiNO_3$ solubilizers such as copper fluoride [34], γ-butyrolactone [35], and Tin trifluoromethanesulfonate [36], tris(pentafluorophenyl)borane [37] into carbonate electrolytes to improve the solubility of $LiNO_3$. However, these $LiNO_3$ solubilizer additives also destabilize the SEI, as evidenced by a lower Li plating/stripping CE of <99% than that (99.3%) [38] of highly concentrated or all-fluorinated LiFSI (or $LiPF_6$) single-salt carbonate electrolytes [39]. Therefore, $LiNO_3$ solubilizers that do not jeopardize the SEI in carbonate electrolytes should be further explored.

Here, we used the solvent dimethyl sulfoxide (DMSO) as a $LiNO_3$ solubilizer to form an additive solution of 4.0 M $LiNO_3$ in DMSO, and added it into 0.8 M $LiPF_6$ FEC/DMC (1:4 by vol.) at 5 wt% to form the $LiNO_3$ saturated electrolyte (denote as $LiNO_3$-S). In the $LiNO_3$-S electrolyte, NO_3^- participates in the primary Li^+ solvation sheath at high concentration, enabling NO_3^- ions to form the aggregates structure. The aggregates solvation structure promotes the preferential reduction of NO_3^- to form an inorganic-rich SEI, which can effectively suppress Li dendrite formation and increases the Li plating/stripping CE to a recorded high value of 99.55% at a current of 1.0 mA cm^{-2} and a capacity of 1.0 mAh cm^{-2}. The 99.55% CE for Li plating/stripping in $LiNO_3$-S carbonate electrolytes is the highest CE in all reported carbonate electrolytes, and is even comparable to the recorded value (99.5%) of local high-concentrated ether electrolytes [40]. By leveraging the high anodic stability of carbonate electrolytes, $LiNi_{0.8}Mn_{0.1}Co_{0.1}O_2$ (NCM811)||Li full cells with a high areal capacity of 2.5 mAh cm^{-2} and a limited Li excess anode (50μm) was also evaluated in the designed electrolytes and demonstrated a 75% capacity retention after 200 cycles (with nearly tripled the cycling lifespan), which is extremely appreciable in carbonate electrolytes.

Results and Discussion

Solvation structure and properties of the carbonate electrolyte with $LiNO_3$ additive

The solubility of $LiNO_3$ in both EC/DMC and FEC/DMC electrolytes is very low, as evidenced by a distinct $LiNO_3$ sediments at the bottom of both solutions after only 1.0 wt% $LiNO_3$ was added. (**Figure S1a, b)**. The donor number (DN) chemistry [41] has been used to predict the ability to dissociate salts with ion pairs, and a parameter to describe the Lewis basicity of solvents. Basically, the larger the DN value, the better the solvent solubilizes salts. As shown in **Figure S2**, the DN of EC (16), DMC (17) and FEC (9) are much lower than that of NO_3^- (22) [41-44]. Therefore, the solubility of $LiNO_3$ in carbonate solvents is very low. DMSO has a much higher DN number (30) [45] and the $LiNO_3$ solubility in DMSO is at least two orders of magnitude higher (more than 4000 mM at 25°C) than that for carbonate electrolytes.

In the high-concentrated 4.0 M $LiNO_3$-DMSO nitrate solution, free DMSO molecules are far fewer than in dilute solution (<1.0 M), and the interionic attractions are pronounced. The unique solvation structure of high-concentrated nitrate electrolytes also increases the viscosity of the bulk electrolyte and changes the SEI compositions on the anodes, as demonstrated in the "water-in-salt" aqueous electrolytes [46-47] as well as highly concentrated organic electrolytes [38, 48]. Therefore, antisolvents need to be added into these highly concentrated organic electrolytes in order to reduce their viscosities [39, 49]. In this work, we added a small amount of 4.0 M $LiNO_3$-DMSO solution into dilute carbonate electrolytes to leverage merits of both electrolytes while minimizing their weaknesses. To our best knowledge, using a solvent-in-salt solution as an additive to manipulate the SEI composition in dilute electrolytes for LMBs has remained unexplored, which provides a new opportunity to design

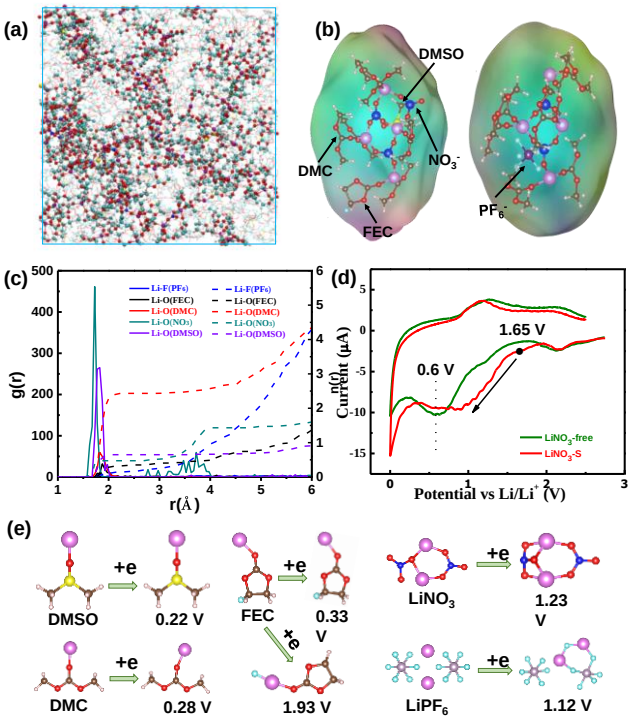

Figure 1. MD Simulation and decomposition potential for the $LiNO_3$-S electrolyte. (a) The snapshot of the MD simulated box. Li^+ ion and coordinated molecules (within 3.5 Å of Li^+ ions) are depicted by a ball-and-stick model, while the wireframes stand for the free solvents; (b) Representative Li-solvation structure with NO_3^- involved and (c) radial distribution function (g(r), solid lines) and coordination numbers (n(r), dashed lines) of $LiNO_3$-S electrolyte; (d) Typical CV curves of Li||Cu half cells scanned between 0 V-2.5 V at 0.1 mV s^{-1} in different electrolyte; (e) Optimized Li^+-solvent, $(LiNO_3)_2$, and $(LiPF_6)_2$ complexes from M052X calculations using SMD (ε=20) implicit solvation model. Calculated reduction potential vs. Li/Li^+ are listed next to each complex).

electrolytes.

The 1.0 M $LiPF_6$ in FEC/DMC (1:4 by vol.) solution was chosen as the base electrolyte (denoted as $LiNO_3$-free electrolyte) because it is one of the best carbonate electrolytes for lithium ion batteries [50-51]. For comparison, $LiNO_3$-DMSO solutions with varying $LiNO_3$ salt concentrations were added to $LiPF_6$ FEC/DMC electrolytes. Due to the "common-ion effect", the $LiPF_6$ concentration was reduced to 0.8 M in order to promote the better

$LiNO_3$ compatibility. As shown in **Figure S1c**, no precipitation is observed in the electrolyte, even when 5 wt% of 4 M $LiNO_3$-DMSO was added to the 0.8 M $LiPF_6$ FEC/DMC electrolyte, suggesting the excellent solvating power of DMSO for $LiNO_3$. Here, M represents mole of salt dissolved in a liter of solvent.

Classic molecular dynamic (MD) simulations were performed to understand the solvation structures of these electrolytes. For the $LiNO_3$-free electrolyte (**Figure S3**), the carbonate molecules, including FEC and DMC, are the major component in the primary Li^+ solvation sheath. In such carbonate electrolytes, reduction of solvents is preferred with much higher potentials than that of Li metal deposition, resulting in a highly organic-rich SEI with strong lithiophilicity. However, in $LiNO_3$-S electrolyte (0.8 M $LiPF_6$ FEC/DMC with 5 wt% (4 M $LiNO_3$-DMSO)), ions are distributed uniformly throughout the electrolyte as evidenced by the representative snapshot of the $LiNO_3$-S electrolyte (**Figure 1a**). The representative Li solvation structures in **Figure 1b & Figure S4** indicate that distinct NO_3^- ions are involved in the solvation sheath while small anoumt of DMSO molecules are found. The radial distribution functions show apparent peaks around 1.8 Å, indicating the primary Li^+ solvation sheath with NO_3^- anion participation (**Figure 1c**). The coordination numbers for PF_6^-, NO_3^-, DMC, DMSO and FEC were found to be 0.24, 0.50, 2.43, 0.66, and 0.40, respectively. Although the 99.7 % of the DMSO are in the Li first solvation shell, the low concentration of DMSO in the mixed electrolyte limits its ratio in the solvation structure. Interestingly, each NO_3^- anion is found to solvate with an average of 2.63 Li^+ ion (**Figure S5**), indicating the successful formation of the aggregates structure, which has been widely observed in highly concentrated electrolytes. The MD simulations indicate that the aggregates structure in the 4 M $LiNO_3$-DMSO (**Figure S6**) can be maintained even when it is dissolved into the 0.8 M $LiPF_6$ in FEC/DMC electrolyte. Meanwhile, the Raman spectra of the DMSO solution and carbonate electrolytes with different $LiNO_3$ concentrations were further studied in **Figure S7**. As shown in **Figure S7a**, the pure DMSO displays two typical peaks at 672 cm^{-1} and 703 cm^{-1}, which correspond to the C-S-C symmetric asymmetric stretching of DMSO. When $LiNO_3$ is dissolved in DMSO solvent, the two peaks are maintained in the spectrogram but shift to the higher value, which reaches 678 cm^{-1} and 710 cm^{-1} in the 4M $LiNO_3$-DMSO solution. This is mainly because increasing the $LiNO_3$ concentration can promote Li^+-solvated DMSO structure as well as the association of Li^+ ions with NO_3^- ions, thus reducing the free DMSO.[52] The similar trend is also find in the FEC-based carbonate electrolyte with various concentrated $LiNO_3$-DMSO additive (**Figure S7b**), which further confirms the participation of NO_3^- ions in the Li^+ solvation structure and the enhanced the coordination strength under improved concentration.

The reduction potentials of $LiNO_3$-S and $LiNO_3$-free electrolytes were also evaluated using cyclic voltammetry (CV) at a scanning rate of 0.1 mV s^{-1} in a potential range from 2.5 V to 0.0 V to avoid Li metal deposition during redox of $LiNO_3$. As shown in **Figure 1d**, the $LiNO_3$-S electrolyte shows a distinct reduction slope from 1.65 V to 1.0 V during the cathodic scan, which is similar to the pure 4 M $LiNO_3$-DMSO solution (**Figure S8).** The reduction slop between 1.65 V to 1.0 V is attributed to a cathodic reduction of $LiNO_3$ [53]. Therefore, the $LiNO_3$ is reduced in the first discharge process forming the SEI and preventing further reduction of $LiNO_3$ in the following cycles. Meanwhile, the cathodic peak around 0.6 V for $LiNO_3$-free electrolytes is attributed to the reduction of the carbonate solvent [10, 54], which disappears in the $LiNO_3$-S electrolyte, indicating that the SEI formation from reduction of $LiNO_3$ suppress carbonate reduction at 0.6V. The small peak around 2.1 V for both electrolytes can be assigned to the reduction of the inevitable copper oxide on Cu electrode surfaces [55].

To further uncover the mechanism, the reduction of the Li-solvent, $LiNO_3$, and $LiPF_6$ were studied using quantum chemistry (QC) calculations. **Figure 1e** shows the optimized structures of solvents and salts before and after reduction and the corresponding reduction potentials. FEC and $LiPF_6$ ion pairs thermodynamically defluorinate at 1.93 V and 1.12 V, respectively, forming LiF, which is in consistent with previous work [56]. However, the FEC ring deformation kinetically prefers a one electron transfer around 0.33 V before Li^+ (or Li metal) coordinates with the fluorine atom of FEC and reduces into LiF [57]. Therefore, the inorganic LiF in the inner SEI primarily results from $LiPF_6$ reduction. Since the reduction potential of the $LiNO_3$ dimer (1.23 V) is higher than that of the $LiPF_6$ dimer (1.12V), $LiNO_3$ will be reduced first during potential decrease, as confirmed by the CV scan (**Figure 1d**). The reduction potentials of other Li-solvent complexes are much lower than 1.0 V. In summary, NO_3^- has participated in the primary solvation sheath of Li^+ forming the aggregates solvation structures when the $LiNO_3$-DMSO additive is combined with the carbonate electrolyte. The preferential reduction of $LiNO_3$ and $LiPF_6$ salts enables the formation of an inorganic LiF, Li_2O, Li_3N, and other nitrides inner SEI layer with an organic outer SEI layer from later solvent reduction.

Li plating/stripping in $LiNO_3$-S and $LiNO_3$-free electrolytes

The Li plating/stripping CE on a bare Cu substrate in the electrolytes with various concentrations of $LiNO_3$ additive was evaluated by a galvanostatic Li plating/stripping test. To mimic the Li plating/stripping cycles of a Li excess anode and minimize the impact of the Cu substrate, a special CE measurement protocol [58] was used here. Prior to cycling, Cu substrate was conditioned by plating 3 mAh cm^{-2} of Li metal on the Cu substrate and then the plated Li was fully stripped to 0.5 V. Afterwards, a total capacity of the Li reservoir (Q_T = 3 mAh cm^{-2}) was deposited back on the stabilized Cu substrate again at a current of 1.0 mA cm^{-2}. After that, one third of plated Li (Q_C= 1 mAh cm^{-2}) was stripped/plated in each cycle at the same current density of 1.0 mA cm^{-2}. Finally, the Li remaining after 10 Li plating/stripping cycles was completely stripped to 0.5 V at 1.0 mA cm^{-2} to calculate the cycling CE. As shown in **Figure 2a** the Li nucleation overpotential is reduced and the CE is increased with increasing $LiNO_3$ concentration in DMSO. The peak overpotential (inset in **Figure 2a**) represents the nucleation overpotential to overcome the heterogeneous nucleation barrier of metallic Li on Cu surfaces. With the addition of $LiNO_3$, the nucleation potential decreases from 140 mV to 75 mV, suggesting that the $LiNO_3$ additive promotes the formation of a highly Li-ion conductive SEI. Meanwhile, the Li plating/stripping CE increases with the $LiNO_3$ concentration and the $LiNO_3$-S electrolyte has the highest CE of 99.55% at a current of 1.0 mA cm^{-2} and a capacity of 1.0 mAh cm^{-2}, which is one of the best value reported for LMBs in all carbonate electrolyte systems at similar currents and capacities (**Table S1**). In addition, we tested the electrochemical performance of $LiNO_3$-S electrolyte by one-solution route, namely all the solvent and salt compounds are mixed together at once. Its CE can also reach a high value of 99.34% (**Figure S9**) but is a little lower than that of $LiNO_3$-S electrolyte by two-solution route (99.55%). It is possible that the heating process promotes the side reaction between FEC and $LiPF_6$ in $LiNO_3$-S electrolyte by one-solution route, thus generating more impurities in the electrolyte.[59] Meanwhile, experimental error may also cause this subtle difference. Therefore, our two-solution strategy is more convenient in minimizing the errors during electrolyte preparation. The gaseous product of Li||Cu cell in $LiNO_3$-S electrolyte after the cycling was also studied by mass spectrometer (MS), which confirms there is almost no N-contained gas generated and thus no serious gas concern in our designed electrolyte (**Figure S10**). It is possible that $LiNO_3$ is directly reduced to Li_2O and Li_xNO_y to form the SEI on Li metal surface or the resulted N_2 and N-O gas further react with metallic Li to create Li_3N and Li_xNO_y,[32, 60] thus almost no N-contained gas has been tested in our electrolyte. The specific SEI components will be discussed by the next part in detail.

The cycling stability of Li anodes highly depends on the CE and Li utilization in each cycle. In practical LMBs, Li metal normally is not fully removed from the current collector and there are always excess Li remained on the anode [61]. The theoretical capacity retention (Q_R) at a certain CE and Li utilization (Qc/Q_T) can be calculated using the followed equation: $Q_R = Q_T - n(1-CE)Q_C$. If the

Li metal utilization is 33.3% (Q_C/Q_T), the calculated capacity drops with Li plating/stripping cycles as shown in **Figure S11,** which clearly demonstrates the importance of CE for long-term cycling stability. **Figure 2b** shows that Li anodes in the $LiNO_3$-free electrolyte can only survive for 41 cycles even at a low Li utilization of 33% due to a CE of 97%. By contrast, the Li anodes in the $LiNO_3$-S electrolyte exhibits a stable cycling profile for 100 cycles without any obvious voltage polarization increase. The Li CE after 100 cycles is still maintained as high as 99.42%. At a high capacity of 2 mAh cm^{-2}, the Li CE in the $LiNO_3$-S electrolyte still maintained a high value of 99.16% while it dropped to 96.31% in the $LiNO_3$-free counterpart (**Figure S12**). Li deposition kinetics were further investigated in a Li||Cu half-cell using CV in the potential range of -0.3 V-0.6 V (**Figure 2c**). The Li plating/stripping currents in the $LiNO_3$-S electrolyte are much larger than in the $LiNO_3$-free electrolyte, demonstrating fast reaction kinetics. Moreover, the nucleation onset potential in the $LiNO_3$-S electrolyte is decreased by 44 mV compared to that in the $LiNO_3$-free electrolyte, further confirming the high reaction kinetics for Li deposition in the $LiNO_3$-S electrolyte.

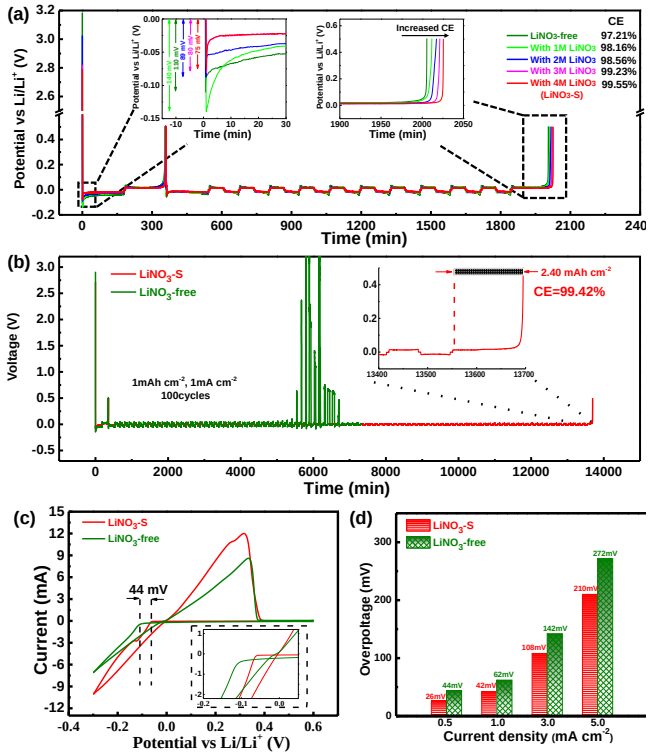

Figure 2. Li plating/stripping performance in various electrolytes. (a) Li plating/stripping CE in Li||Cu cells in electrolytes with different concentrations of $LiNO_3$ at a current density of 1 mA cm^{-2} and a capacity of 1 mAh cm^{-2}. The insets are magnified view of the Li nucleation potential and final stripping capacity in various electrolytes. (b) The Li plating/stripping voltage during long-term cycling; (c) CV curves for Li plating/stripping between -0.3 V-0.6 V at a scan rate of 2 mV s^{-1}; (d) Polarization comparison of Li plating/stripping in $LiNO_3$-S and $LiNO_3$-free electrolytes at different current densities.

The electrochemical impedance spectroscopy (EIS) evolution in the Li||Li symmetrical cell can also be utilized to evaluate the interfacial dynamics of the Li metal anode. It is generally accepted that the semicircle in the high-frequency region is attributed to the Li-ion diffusion through the SEI (R_{SEI}). As displayed by the Nyquist plots in **Figure S13a**, the R_{SEI} in the $LiNO_3$-free electrolyte has an initial impedance of around 125 Ω, and this value increases to nearly 175 Ω after a 15 h rest due to growth of the SEI. A similar impedance increase is found in the $LiNO_3$-S electrolyte (**Figure S13b**). By contract, the SEI resistance of Li is very small and stable in the $LiNO_3$-S electrolyte with only a minor increase from 20 Ω to 26 Ω (nearly one seventh of the $LiNO_3$-free electrolyte) after the same resting step, which further proves that the $LiNO_3$ additive forms a thin and dense SEI with a higher Li-ion conductivity. Such a stable SEI in the $LiNO_3$-S electrolyte with a low interfacial resistance is beneficial for promoting the uniform Li deposition and suppressing the dead Li formation during cycling. Specifically, the rate performance under a capacity of 1.0 mAh cm^{-2} in symmetrical Li cells in two electrolytes were also compared in **Figure S14a**. Generally, the voltage hysteresis in both electrolytes increased with current density owing to the increased dynamics resistances, but the overpotential of Li plating/stripping in the $LiNO_3$-S electrolyte was much less than that observed in the $LiNO_3$-free electrolyte. The enlarged view of the overpotential vs. capacity during the entire cycling process is also plotted (**Figure S14b, c**), and the more visualized evolution of the average overpotential between Li plating/stripping at different current densities is presented in **Figure 2d**. Impressively, a much smoother voltage plateau (**Figure S14b**) with small polarizations of 26, 42, 108, and 210 mV at 0.5, 1.0, 3.0, and 5.0 mA cm^{-2}, respectively, were observed in the $LiNO_3$-S electrolyte, which are all far below the values of the $LiNO_3$-free electrolyte. Such a great stability enhancement is definitely stemmed from a more stable SEI with reduced impedance for the uniform Li plating/stripping and improved charge transfer kinetics. By contrast, the cell overpotential in the $LiNO_3$-free electrolyte shows irregular voltage hysteresis fluctuations with a large overpotential peak at the initial and end of the plating/stripping process (**Figure S14c**). The strong bonding between Li and the organic-rich SEI is responsible for the high initial overpotential. This becomes smaller after SEI cracking occurs due to the huge volume expansion occurring during Li plating, while the reformation/growth of SEI at the end of Li deposition increases the overpotential again. As a result, the repeated breaking/reformation of the SEI increase its thickness with higher ionic resistance, which is further confirmed by the larger impedance of cycled Li||Li cells in the $LiNO_3$-free electrolyte than tin $LiNO_3$-S electrolyte (**Figure S15**).

The morphology of deposited Li metal was also evaluated by scanning electron microscopy (SEM). After plating 3 mAh cm^{-2} of Li on Cu substrates at 1 mA cm^{-2}, coin cells were disassembled for microscopic analysis. The typical diagrams for Li morphologies in $LiNO_3$-free and $LiNO_3$-S electrolytes have been displayed in **Figures 3a** and **3d**, respectively. As revealed in **Figure 3b**, nodule-like Li, rather than whiskers, is found on top of plated Li in the $LiNO_3$-free electrolyte, which is in agreement with previous reports that the FEC-rich electrolyte can generate a LiF-contained SEI enabling blocky Li growth [62-63]. However, the plated Li is separated and stacked with each other, forming porous Li, and thus reducing CE under continuous cycling. The deposited Li in the $LiNO_3$-free electrolyte also manifests as a loosely packed structure, resulting in a ~19.5 μm-thick Li layer from the cross-section image (**Figure 3c**). In stark contrast, the top-view image of the deposited Li in the $LiNO_3$-S electrolyte shows a dense surface with rounded edges tightly connected as a dense layer under the protective layer (**Figure 3e**), which displays a smaller thickness of ~14.8 μm due to its compact structure (**Figure 3f**). The inserted optical pictures in **Figures 3b** and **3e** also clearly demonstrate that the electrodeposited of Li in the $LiNO_3$-S electrolyte has a silver-white color, closer to the pristine Li metal,

indicating that the derived SEI is more stable at preventing side reactions with Li metal. In contrast, the electrodeposited Li in the $LiNO_3$-free electrolyte is darker. More vivid evolution of the morphology with the increased areal capacity was further revealed by additional SEM images (**Figure S16**). It is shown that the deposited Li gradually grows into the intimate aggregates without porosity in the $LiNO_3$-S electrolyte while the loose Li structure with smaller particles is shown in the $LiNO_3$-free electrolyte. It was reported that a high CE can be achieved when chunky Li is deposited with low tortuosity and intimate connection to maintain the bulk integrity.[19] Since the side reactions between the deposited Li and the $LiNO_3$-S electrolyte have been greatly reduced, an outstanding CE with a Li metal anode has been achieved.

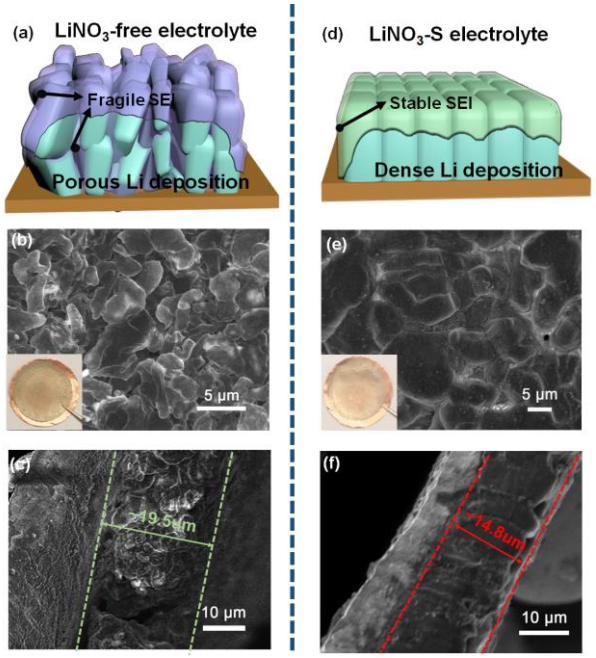

Figure 3. Schematic diagrams and typical SEM images of the plated Li morphology. Metallic Li is electrochemically deposited (1 mA cm^{-2}, 3 mAh cm^{-2}) on the bare Cu substrate in the (a-c) $LiNO_3$-free electrolyte and (d-f) $LiNO_3$-S electrolyte.

Characterization of the inorganic-rich SEI

The SEI compositions formed in the $LiNO_3$-S electrolyte and the $LiNO_3$-free electrolyte were characterized by in-depth X-ray photoelectron spectroscopy (XPS) with continuous Ar-ion sputtering from the surface to the bottom (closer to the Li metal). **Figures 4a-d** display the SEI composition on the Li anodes after 20 plating/stripping cycles (1 mA cm^{-2}, 1 mAh cm^{-2}) in $LiNO_3$-S and $LiNO_3$-free electrolytes. The cycled Li was transferred under an inert Ar atmosphere to avoid any contamination by air or moisture. For the indicative C 1*s* spectrum, the organic components derived from carbonate solvents exist in both SEI layers. The top surface of the SEI formed in the $LiNO_3$-free electrolyte has a much stronger C-O peak, initially around 286.5 eV, and the C-H/C-C (284.6 eV) intensity persists without distinct attenuation during the whole 600 s sputtering (**Figure 4a**), indicating organic compounds are enriched from the surface to the inner part. Clear organic species are also found in the upper SEI formed in the $LiNO_3$-S electrolyte, such as -CO_3- and C-O groups, which may serve as the connectors of SEI to withstand the volume change during cycling.[64] However, all these C 1s signals, especially C-C/C-H and -CO_3- peaks, drop sharply after 300 s of etching (**Figure 4c**), which demonstrates much less organic reduction species in the inert part of the SEI. For the F 1s spectrum, the specific LiF and Li_xPF_y signals are also observed in both electrolytes, which results from the decomposition of $LiPF_6$ salt and FEC solvent [50]. LiF has been well-known as an excellent SEI component for its high interfacial energy with Li metal and high mechanical strength, thus it is effective at suppressing dendrite growth and enabling uniform Li deposition. Therefore, FEC-based carbonate electrolytes usually exhibit better Li metal performance than EC-based ones. For the SEI in the $LiNO_3$-S electrolyte, the inorganic $LiNO_2$, LiN_xO_y, Li_3N, and Li_xN_y species are present, suggesting that $LiNO_3$ has been reduced to form the resulting SEI. Besides, Li_3N is a lithium super ionic conductor [65], which can help enhance the ion transport property of the SEI. More importantly, the Li_2O content from the O 1*s* spectrum is significantly improved especially after deeper etching, which reveals that the decomposition of $LiNO_3$ also helps to promote more inorganic Li_2O grains in the resulting SEI. As we discussed early for the solvation structure of the $LiNO_3$-S electrolyte, $LiNO_3$ is prone to being reduced at a higher potential, and thus contributes more inorganic ceramics to the inert SEI close to Li metal when compared with the carbonate solvent. Meanwhile, no clear S signal is found in the S 2*p* spectrum (**Figure S17**), clearly demonstrating no signifcant side reactrion of DMSO due to the effective stabilization of Li metal anode by $LiNO_3$ additive in the $LiNO_3$-S electrolyte, which is in good agreement with solvation structure analysis.

Figures 4b and **4d** compare the atomic composition ratios in the SEI at different etching times. As shown in **Figure 4b**, the C atomic signature, as an indicator for organic components, is the highest among all elements on the SEI surface. Therefore, more organic species were observed in the outer layer of the SEI after cycling in the reference $LiNO_3$-free electrolyte. With the etching, the organic species gradually decreased, but still maintained a high percentage of 15.6% after 600s of sputtering, indicating polymer is still enriched in the entire SEI. In sharp contrast to **Figure 4d**, the C ratio is sharply decreased to only 5.2% while the total of the Li and O ratios reached an ultrahigh value of 81.6% after 600s of sputtering, confirming that a highly inorganic-rich inner SEI layer on Li is obtained in the $LiNO_3$-S electrolyte. It needs to mention that the outer organic component may be reduced by the electron leakage due to the defects in the inner SEI layer such as radicals[66], interstitials[67], and polarons[68]. But nonetheless, much more inorganic species are still concentrated in the SEI layer formed in the $LiNO_3$-S electrolyte, both on the surface as well as in the bulk. Specifically, inorganic species, taking Li and O elements as the indicators, always occupy the major components of the outer SEI layer. Meanwhile, the atomic ratios of F and N elements exhibit no huge fluctuation during the entire sputtering, indicating the relatively homogeneous fluoride and nitride distribution in the resulting SEI at different depths.

The more detailed morphology and structure of the SEI formed in the $LiNO_3$-S electrolyte was further characterized by time-of-flight secondary ion mass spectroscopy (ToF-SIMS). As shown in **Figures 4e** and **4f**, the edge surface of the crater presents an explicit etching layer of around 130 nm thickness after sputtering with an Ga^+ ion beam (20 μm × 20 μm area). In the negative mode, significantly strong contents of O, F, and certain amounts of N and NO groups were found within the top 40 nm surface layer (**Figure 4g**), which reveals the thickness of the formed SEI. The O signal aggregates with a distinct distribution because $LiNO_3$ in the $LiNO_3$-S electrolyte is preferentially reduced to form Li_2O and suppresses the reduction of the carbonate solvent molecules (forming polycarbonate). The structural information of the SEI components were further detected by high-revolution transmission electron microscopy (HTEM) using a cryogenic temperature stage owing to the fragile property of the electrode interphase. Li metal was directly deposited on a Cu TEM grid for a convenient cryotransfer protocol. Abundant polycrystalline inorganics with various lattice spacings, mainly matching the planes of Li_2O and Li_2CO_3, can be clearly identified as well as the

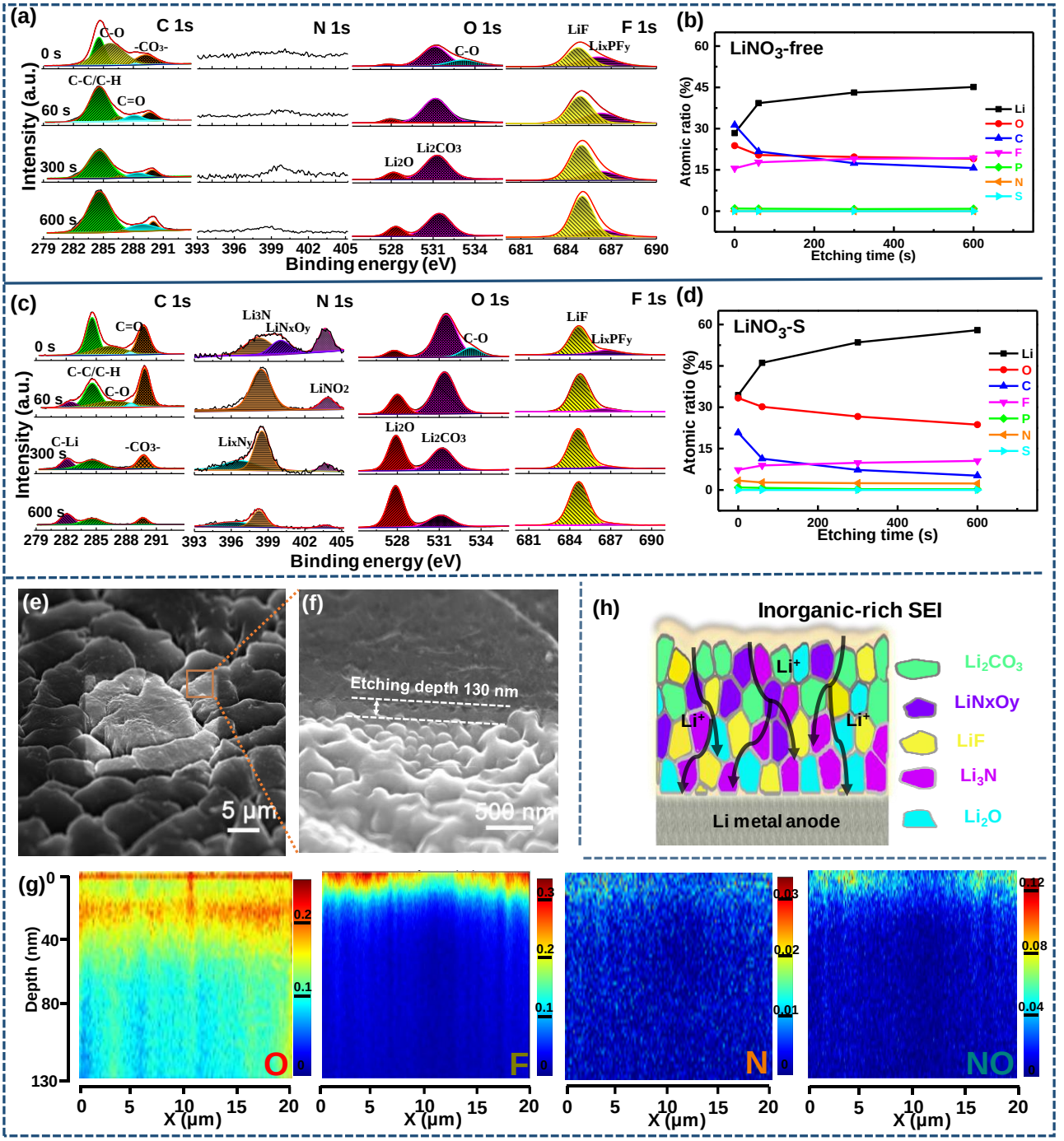

Figure 4. The in-depth structure characterization of the SEI on the Li metal surface. (a-d) The typical elemental spectra and the atomic composition ratios by XPS measurement of the SEI layer formed in (a, b) $LiNO_3$-free and (c, d) $LiNO_3$-S electrolyte. The binding energy was calibrated with C 1s at 284.6 eV and a Shirley BG type was used for background subtraction. Both peak deconvolution and assignments in C1s, O1s, N1s, and F1s spectra are presented. (e-g) The interface analysis of the deposited Li metal in the $LiNO_3$-S electrolyte by ToF-SIMS: (e,f) The crater with a magnified image of around 130 nm sputtered by a Ga^+ ion beam and (g) the corresponding O, F, N, and NO distributions in the sputtered cross section. (h) The structure schematic of the inorganic-rich SEI formed in the $LiNO_3$-S electrolyte for uniform Li deposition.

existing amorphous structure. Specifically, the Li_2O species are more distributed on the inner side of the SEI, forming large amounts of heterogeneous grain boundaries spatially (**Figure S18a**). Although no fluoride or nitride crystalline phases was observed by HTEM, the existence of crystalline LiF, Li_2O and Li_3N in SEI was confirmed by the electron patterned diffraction (**Figure S18b**). Meanwhile, the elements O, F and N have been captured over the entire region via an elemental mapping with an energy dispersion spectrum (**Figure S19**).

Based on the discussion above, we can infer that the $LiNO_3$ additive has effectively altered the spatial distribution of inorganics as well as its components in the SEI in the FEC-based carbonate electrolyte. Despite traces of solvent molecules inevitably participating in the SEI formation, the addition of $LiNO_3$ promotes the generation of much more Li_2O and N-containing components in the interface with bulk Li metal. The SEI mainly

consists of stacked inorganic compounds as shown in **Figure 4h**, where inorganic nanocrystallites are dispersed throughout the amorphous matrix. It mainly displays an abundant distribution of inorganic particles, in which Li_2O, Li_3N, and LiF are more enriched at the metallic Li interface, with more Li_2CO_3, LiN_xO_y, and LiF next to it, and an organic layer on the electrolyte side of the SEI. Moreover, the highly ordered crystals with directional layout and large grain boundaries can significantly affect the Li-ions' diffusion through the SEI, and what needs to be mentioned is that the amorphous area may also be composed of inorganic components (with trace organic polymer based on the ultralow C content). As a result, those inorganic components (including LiF, Li_2O, LiN_xO_y, and Li_3N) dominate the main constituents of the interphase layer, and thus, enable the advanced and inorganic-rich SEI to display high interfacial energy, outstanding mechanical properties, and ion-transport capabilities.

Performance of Li||NMC811 full cells

The Li||NMC811full-cell performance with $LiNO_3$-S and $LiNO_3$-free electrolytes was also compared using a ~50 μm Li metal anode and NMC811 cathode at an areal capacity of 2.5 mAh cm^{-2}. The electrochemical oxidation window of the electrolytes was firstly evaluated on stainless steel electrodes using a linear sweep voltammetry (LSV). As shown in **Figure S20**, the $LiNiO_3$-S electrolyte shows an oxidative stability potential of > 4.5 V. Moreover, the CV curve of Li||NMC811 cells in the $LiNO_3$-S electrolyte exhibit three charactistic peaks (**Figure S21)**, representing the typical phase transitions for the NMC cathode. Therefore, the $LiNO_3$-S electrolyte is compatible with the high-voltage nickel-rich cathode. The long-term cycling stability of Li||NMC811 cells was investigated at 0.5 C after two formation cycles at 0.1 C (**Figure 5a**). The Li||NMC811 cell with the $LiNO_3$-free carbonate electrolyte showed continuous capacity decay during the charge/discharge cycles with an abrupt drop in both capacity and CE around the 80^{th}-85^{th} cycles. In contrast, an improved cycling performance with almost triple the lifespan was achieved using the $LiNO_3$-S electrolyte with a high capacity retention of 75% after 200 cycles and an outstanding CE of 99.83% with no sign of any dramatic change. The voltage-capacity profiles in **Figures 5b** and **5c** show that the cell discharging capacity in the $LiNO_3$-free electrolyte dropped to 1.22 mAh cm^{-2} after 100 cycles, while the Li-NMC811 cell with the $LiNO_3$-S electrolyte maintains a capacity of 2.15 mAh cm^{-2}. In addition, cell discharge voltage in the $LiNO_3$-free electrolyte also decreased faster than that in the $LiNO_3$-S electrolyte, indicating that the sustainability of the SEI is greatly enhanced by the $LiNO_3$ additive.

It needs to emphasize that the inorganic-rich SEI formed in $LiNO_3$-S electrolyte is always presented on the surface of Li metal anode at different cycles (**Figure S22** and **Figure S23**). Due to the high interfacial energy, outstanding mechanical property and ion-transport capability, the inorganic-rich SEI effectively suppresses the dendrite formation and improves the Li CE, thus enabling the excellent performance of Li||NCM811 cell with limited Li excess. By comparison, a much more organic-rich SEI is formed on Li metal surface of Li||NCM811 cell after cycling in $LiNO_3$-free electrolyte (**Figure S24**), similar to the XPS results in Li symmetric cells (Figure 4a-b). To further uncover the kinetic features of the electrode interface, EIS of the Li||NCM811 cells after various cycles were also carried out (**Figure S25**). The Nyquist plots of the cells always contain one semicircle at high frequencies, which are connected with Li^+ transfer through the interface and its specific resistance can be measured by the radius value. Generally, the interfacial resistance increased from the initial to the later cycles in both $LiNO_3$-free and $LiNO_3$-S electrolyte, which is mainly due to the accumulated thickness of SEI. But compared with the cell in $LiNO_3$-free electrolyte, the Li||NCM811 cell in $LiNO_3$-S electrolyte always exhibits a smaller total interfacial resistance with the slower growth rate during the cycling, which can be attributed to the formation of a more stable SEI with faster kinetics.

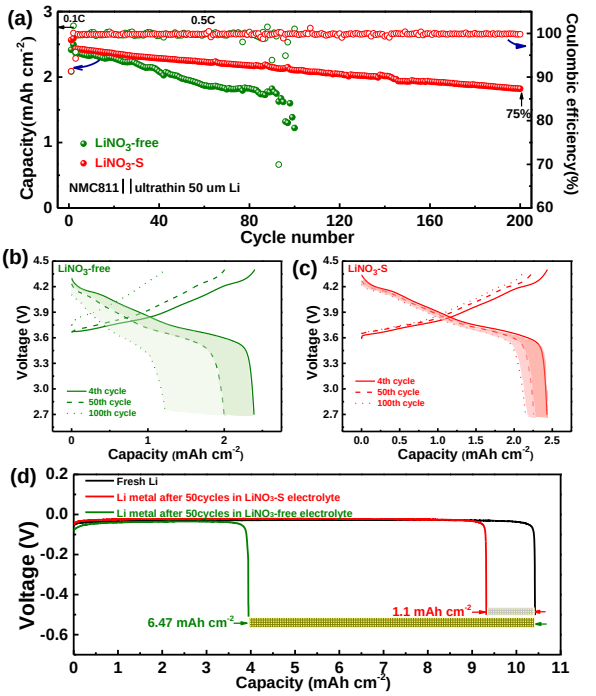

Figure 5. Performances of Li||NCM811 full cell in $LiNO_3$-S and $LiNO_3$-free electrolytes. (a) Cycling performance of Li||NCM811 cells with 50 μm Li at 0.5 C. (b, c) Corresponding charging/discharging profiles of Li||NCM811 batteries after 4, 50, and 100 cycles with (b) $LiNO_3$-free and (c) $LiNO_3$-S electrolytes. (d) The capacity loss of 10.4 mAh cm^{-2} Li after 50 cycles in different electrolytes. Only 1.1 mAh cm^{-2} of Li was lost in the $LiNO_3$-S electrolyte, while a large amount of 6.47 mAh cm^{-2} of Li was lost in $LiNO_3$-free electrolyte after 50 cycles.

Figure S26 shows the morphology of Li metal anodes in Li||NCM811 cells after 50 cycles in both electrolytes. The electrode surface in the $LiNO_3$-free electrolyte (**Figure S26 a**, **b**) has been covered with Li filaments and dendrites, resulting in a quick capacity decay. Meanwhile, the plated Li in the $LiNO_3$-S electrolyte shows a much more uniform and dense morphology with a large granular structure (**Figure S26 c**, **d**). To determine the exact amount of Li loss, a Li||NMC811 cell was disassembled after 50 cycles and then the residual Li in the cycled Li anode was completely stripped to -0.5V in a reassembled Li||Cu cell. As shown in **Figure 5d**, the fresh Li disk delivers a pristine capacity of 10.4 mAh cm^{-2} (black line). The areal Li loss after 50 cycles in the $LiNO_3$-S electrolyte is only 11 mAh cm^{-2}, which is calculated by dividing the capacity difference by the area (1.27 cm^{-2}). However, as high as 6.47 mAh cm^{-2} of Li is lost after 50 cycles in the $LiNO_3$-free electrolyte, which is more than 5 times of active Li consumed by the corrosive carbonate electrolyte under the same cycling conditions. Such a stark difference further demonstrates the importance of high Li metal CE for capacity retention and reveals the great potential of the $LiNO_3$ additive in improving the lifespan of rechargeable LMBs.

The electrochemical performance of LMBs is significantly improved simply by incorporating the $LiNO_3$-DMSO additive in currently used carbonate electrolytes, which is of vital importance to match the high-voltage cathode for higher energy density. What needs to mention is that compared with the reported highly concentrated electrolyte strategy, the 4 M $LiNO_3$-DMSO additive is only added by 5 wt% and thus our designed electrolyte has greater superiorities in lower viscosity, better wettability to electrodes and seporator, and especially lower cost, which shows promising application especially in large scale. To avoid trial-and-

error strategies, the electrolyte design principle of forming an inorganic SEI and on Li anodes and a CEI on high voltage cathodes is highly recommended to facilitate the screening process, especially for selecting less-soluble additives. The electrolytes for Li batteries have to satisfy the following requirements: (i) Since an inorganic SEI has a high interfacial energy with metallic Li, high mechanical stiffness, and rapid ionic diffusion along grain boundaries, the electrolytes should be able to form an inorganic-rich SEI, with at least an inorganic-rich layer is desirable in the inner side which is compactly attached to Li metal anode. (ii) To facilitate the formation of an inorganic SEI, lithium salts with inorganic anions (like nitrate, nitrite, borate, fluoroborate, etc.) without organic hydrocarbon groups are suggested as the additive, of which the oxidation potential also needs to be higher than the carbonate solvents. (iii) For additive salts with extremely low solubility in carbonate electrolytes, cosolvents with higher polarity and donor number can be used to promote dissociation. However, to restrain the side reaction of the co-solvent with metallic Li, the concentration of additive salts in the co-solvent should be as high as possible, which can help to increase the lowest unoccupied molecular orbital (LUMO) of the co-solvent for better stability. Besides, such a "concentrated additive" design also favors the anion of the additive to bond more Li^+, promoting the formation of anion aggregates structure with easier decomposition. (iv) Multi-functional additives or the synergistic effect of multiple additives (wide temperature range and low flammability) should also be considered for rechargeable LMBs, especially for larger cells.

Conclusion

In summary, an inorganic-rich SEI was constructed on Li metal anodes by adding small amounts of $LiNO_3$ saturated DMSO into FEC-based carbonate electrolytes. The Li^+ coordination structure with NO_3^- and PF_6^- favored the formation of Li_2O, Li_3N, LiN_xO_y, and LiF abundant SEI layers, which increased the interfacial energy and improved the ionic diffusion as well as the mechanical property of the SEI. The lithiophobic inorganic-rich SEI can effectively suppress the Li dendrite formation and regulate Li deposition as demonstrated by the theoretical analysis and experimental results. Consequently, we increased the Li plating/stripping CE on the Cu substrate up to 99.55% at 1.0 mA cm^{-2} of 1.0 mAh cm^{-2}, which is the highest value ever reported for carbonate electrolytes. The electrolyte can support a high-voltage NCM811 cathode, and 50 μm Li||NMC811 cells achieved an outstanding CE of 99.83% over 200 cycles at a practical areal capacity of 2.5 mAh cm^{-2}. The concentrated $LiNO_3$ additive strategy reported here could also provide new guidelines on the development of future advanced high-voltage LMBs in carbonate electrolytes.

Acknowledgements

This work was supported the Department of Energy (DOE) Office of Energy Efficiency and Renewable Energy (EERE) through Battery500 Consortium under contract No. DE-EE0008202. We acknowledge the University of Maryland supercomputing resources (http://hpcc.umd.edu) made available for conducting DFT computations in this paper. We also thank the Maryland NanoCenter and its AIMLab for support.

Conflict of interest

The authors declare no competing financial interest.

Keywords: lithium metal batteries • carbonate electrolyte• lithium nitrate • electrode interphase • dendrite-free

REFERENCES

[1] G. G. E. Heng Zhang, Xabier Judez, Chunmei Li, Lide M. Rodriguez-Mart&nez, and Michel Armand, *Angew. Chem. Int. Ed.* **2018**, *57*, 15002 – 15027.
[2] J. B. Goodenough, K. S. Park, *J. Am. Chem. Soc.* **2013**, *135*, 1167-1176.
[3] X.-B. Cheng, C. Yan, X.-Q. Zhang, H. Liu, Q. Zhang, *ACS Energy Lett.* **2018**, *3*, 1564-1570.
[4] W. Xu, J. Wang, F. Ding, X. Chen, E. Nasybulin, Y. Zhang, J.-G. Zhang, *Energy Environ. Sci.* **2014**, *7*, 513-537.
[5] X. B. Cheng, R. Zhang, C. Z. Zhao, Q. Zhang, *Chem. Rev.* **2017**, *117*, 10403-10473.
[6] K. N. Wood, M. Noked, N. P. Dasgupta, *ACS Energy Lett.* **2017**, *2*, 664-672.
[7] M. D. Tikekar, S. Choudhury, Z. Tu, L. A. Archer, *Nat. Energy* **2016**, *1*, 16114.
[8] H. Yu, J. Zhao, L. Ben, Y. Zhan, Y. Wu, X. Huang, *ACS Energy Lett.* **2017**, *2*, 1296-1302.
[9] K. Xu, *Chem. Rev.* **2004**, *104*, 4303−4417.
[10] K. Xu, *Chem. Rev.* **2014**, *114*, 11503-11618.
[11] E. Peled, *J. Electrochem. Soc.* **1979**, *126*, 2047-2051.
[12] J. Zheng, J. Yin, D. Zhang, G. Li, D. C. Bock, T. Tang, Q. Zhao, X. Liu, A. Warren, Y. Deng, S. Jin, A. C. Marschilok, E. S. Takeuchi, K. J. Takeuchi, C. D. Rahn, L. A. Archer, *Sci. Adv.* **2020**, *6*, eabb1122.
[13] X. Shen, R. Zhang, X. Chen, X. B. Cheng, X. Li, Q. Zhang, *Adv. Energy Mater.* **2020**.
[14] E. Peled, S. Menkin, *J. Electrochem. Soc.* **2017**, *164*, A1703-A1719.
[15] A. Wang, S. Kadam, H. Li, S. Shi, Y. Qi, *npj Computational Materials* **2018**, *4*, 15.
[16] B. Zhu, Y. Jin, X. Hu, Q. Zheng, S. Zhang, Q. Wang, J. Zhu, *Adv. Mater.* **2016**, *29*, 1603755.
[17] A. A. Assegie, J. H. Cheng, L. M. Kuo, W. N. Su, B. J. Hwang, *Nanoscale* **2018**, *10*, 6125-6138.
[18] L. Suo, Y.-S. Hu, H. Li, M. Armand, L. Chen, *Nat. Commun.* **2013**, *4*, 1481.
[19] C. Fang, J. Li, M. Zhang, Y. Zhang, F. Yang, J. Z. Lee, M. H. Lee, J. Alvarado, M. A. Schroeder, Y. Yang, B. Lu, N. Williams, M. Ceja, L. Yang, M. Cai, J. Gu, K. Xu, X. Wang, Y. S. Meng, *Nature* **2019**, *572*, 511-515.
[20] J. Chen, Q. Li, T. P. Pollard, X. Fan, O. Borodin, C. Wang, *Materials Today* **2020**, doi:10.1016/j.mattod.2020.1004.1004.
[21] X. Fan, X. Ji, F. Han, J. Yue, J. Chen, L. Chen, T. Deng, J. Jiang, C. Wang, *Sci. Adv.* **2018**, *4*, eaau9245.
[22] S. Liu, X. Ji, J. Yue, S. Hou, P. Wang, C. Cui, J. Chen, B. Shao, J. Li, F. Han, J. Tu, C. Wang, *J. Am. Chem. Soc.* **2020**, *142*, 2438-2447.
[23] S. Schweidler, L. de Biasi, A. Schiele, P. Hartmann, T. Brezesinski, J. Janek, *J. Phys. Chem. C* **2018**, *122*, 8829-8835.
[24] X. Q. Zhang, X. B. Cheng, X. Chen, C. Yan, Q. Zhang, *Adv. Funct. Mater.* **2017**, *27*, 1605989.
[25] X. Q. Zhang, X. Chen, X. B. Cheng, B. Q. Li, X. Shen, C. Yan, J. Q. Huang, Q. Zhang, *Angew. Chem. Int. Ed.* **2018**, *57*, 5301-5305.

[26] H. Ota, Y. Sakata, Y. Otake, K. Shima, M. Ue, J.-i. Yamaki, *J. Electrochem. Soc.* **2004**, *151*, A1778-A1788.
[27] X. Ren, Y. Zhang, M. H. Engelhard, Q. Li, J.-G. Zhang, W. Xu, *ACS Energy Lett.* **2017**, *3*, 14-19.
[28] X. Li, M. Banis, A. Lushington, X. Yang, Q. Sun, Y. Zhao, C. Liu, Q. Li, B. Wang, W. Xiao, C. Wang, M. Li, J. Liang, R. Li, Y. Hu, L. Goncharova, H. Zhang, T. K. Sham, X. Sun, *Nat. Commun.* **2018**, *9*, 4509.
[29] Y. Liu, D. Lin, Y. Li, G. Chen, A. Pei, O. Nix, Y. Li, Y. Cui, *Nat. Commun.* **2018**, *9*, 3656.
[30] H. Shin, J. Park, A. M. Sastry, W. Lu, *J. Electrochem. Soc.* **2015**, *162*, A1683-A1692.
[31] R. Elazari, G. Salitra, G. Gershinsky, A. Garsuch, A. Panchenko, D. Aurbach, *Electrochem. Commun.* **2012**, *14*, 21-24.
[32] D. Aurbach, E. Pollak, R. Elazari, G. Salitra, C. S. Kelley, J. Affinito, *J. Electrochem. Soc.* **2009**, *156*, A694.
[33] Q. Shi, Y. Zhong, M. Wu, H. Wang, H. Wang, *Proc. Natl. Acad. Sci. U. S. A.* **2018**, *115*, 5676-5680.
[34] C. Yan, Y. X. Yao, X. Chen, X. B. Cheng, X. Q. Zhang, J. Q. Huang, Q. Zhang, *Angew. Chem. Int. Ed.* **2018**, *57*, 14055-14059.
[35] Y. Jie, X. Liu, Z. Lei, S. Wang, Y. Chen, F. Huang, R. Cao, G. Zhang, S. Jiao, *Angew. Chem. Int. Ed.* **2020**, *59*, 3505-3510.
[36] W. Zhang, Q. Wu, J. Huang, L. Fan, Z. Shen, Y. He, Q. Feng, G. Zhu, Y. Lu, *Adv. Mater.* **2020**, e2001740.
[37] S. Li, W. Zhang, Q. Wu, L. Fan, X. Wang, X. Wang, Z. Shen, Y. He, Y. Lu, *Angew. Chem. Int. Ed.* **2020**, *doi:10.1002/anie.202004853*.
[38] X. Fan, L. Chen, X. Ji, T. Deng, S. Hou, J. Chen, J. Zheng, F. Wang, J. Jiang, K. Xu, C. Wang, *Chem* **2018**, *4*, 174-185.
[39] X. Fan, X. Ji, L. Chen, J. Chen, T. Deng, F. Han, J. Yue, N. Piao, R. Wang, X. Zhou, X. Xiao, L. Chen, C. Wang, *Nat. Energy* **2019**, *4*, 882-890.
[40] X. Cao, X. Ren, L. Zou, M. H. Engelhard, W. Huang, H. Wang, B. E. Matthews, H. Lee, C. Niu, B. W. Arey, Y. Cui, C. Wang, J. Xiao, J. Liu, W. Xu, J.-G. Zhang, *Nat. Energy* **2019**, *4*, 796-805.
[41] S. Sekhon, *Solid State Ionics* **2003**, *160*, 301-307.
[42] N. Nambu, R. Takahashi, M. Takehara, M. Ue, Y. Sasaki, *Electrochemistry* **2013**, *81*, 817-819.
[43] C. M. Burke, V. Pande, A. Khetan, V. Viswanathan, B. D. McCloskey, *Proc. Natl. Acad. Sci. U. S. A.* **2015**, *112*, 9293-9298.
[44] M. I. Gorobets, M. B. Ataev, M. M. Gafurov, S. A. Kirillov, *Journal of Spectroscopy* **2016**, *2016*, 6978560.
[45] H. Pan, J. Chen, R. Cao, V. Murugesan, N. N. Rajput, K. S. Han, K. Persson, L. Estevez, M. H. Engelhard, J.-G. Zhang, K. T. Mueller, Y. Cui, Y. Shao, J. Liu, *Nat. Energy* **2017**, *2*, 813-820.
[46] L. Suo, O. Borodin, T. Gao, M. Olguin, J. Ho, X. Fan, C. Luo, C. Wang, K. Xu, *Science* **2015**, *350*, 938-943.
[47] C. Yang, J. Chen, X. Ji, T. P. Pollard, X. Lu, C. J. Sun, S. Hou, Q. Liu, C. Liu, T. Qing, Y. Wang, O. Borodin, Y. Ren, K. Xu, C. Wang, *Nature* **2019**, *569*, 245-250.
[48] J. Qian, W. A. Henderson, W. Xu, P. Bhattacharya, M. Engelhard, O. Borodin, J. G. Zhang, *Nat. Commun.* **2015**, *6*, 6362.
[49] N. Piao, X. Ji, H. Xu, X. Fan, L. Chen, S. Liu, M. N. Garaga, S. G. Greenbaum, L. Wang, C. Wang, X. He, *Adv. Energy Mater.* **2020**, *10*, 1903568.
[50] E. Markevich, G. Salitra, F. Chesneau, M. Schmidt, D. Aurbach, *ACS Energy Lett.* **2017**, *2*, 1321-1326.
[51] E. Markevich, G. Salitra, K. Fridman, R. Sharabi, G. Gershinsky, A. Garsuch, G. Semrau, M. A. Schmidt, D. Aurbach, *Langmuir* **2014**, *30*, 7414-7424.
[52] N. Togasaki, T. Momma, T. Osaka, *J. Power Sources* **2016**, *307*, 98-104.
[53] S. S. Zhang, J. A. Read, *J. Power Sources* **2012**, *200*, 77-82.
[54] D. Aurbach, H. Gottlieb, *Electrochim. Acta* **1989**, *34*, 141-156.
[55] N. Bellakhal, K. Draou, J. L. Brisset, *J. Appl. Electrochem.* **1997**, *27*, 414-421.
[56] X. Fan, L. Chen, O. Borodin, X. Ji, J. Chen, S. Hou, T. Deng, J. Zheng, C. Yang, S. C. Liou, K. Amine, K. Xu, C. Wang, *Nat. Nanotechnol.* **2018**, *13*, 715-722.
[57] Z. Yang, A. A. Gewirth, L. Trahey, *ACS Appl. Mater. Interfaces* **2015**, *7*, 6557-6566.
[58] B. D. Adams, J. Zheng, X. Ren, W. Xu, J.-G. Zhang, *Adv. Energy Mater.* **2017**, *8*, 1702097.
[59] C. Xu, G. Hernández, S. Abbrent, L. Kobera, R. Konefal, J. Brus, K. Edström, D. Brandell, J. Mindemark, *ACS Appl. Energy Mater.* **2019**, *2*, 4925-4935.
[60] A. Jozwiuk, B. B. Berkes, T. Weiß, H. Sommer, J. Janek, T. Brezesinski, *Energy Environ. Sci.* **2016**, *9*, 2603-2608.
[61] S. Chen, C. Niu, H. Lee, Q. Li, L. Yu, W. Xu, J.-G. Zhang, E. J. Dufek, M. S. Whittingham, S. Meng, J. Xiao, J. Liu, *Joule* **2019**, *3*, 1094-1105.
[62] S. Lin, J. Zhao, *ACS Appl. Mater. Interfaces* **2020**, *12*, 8316-8323.
[63] J. Zhao, L. Liao, F. Shi, T. Lei, G. Chen, A. Pei, J. Sun, K. Yan, G. Zhou, J. Xie, C. Liu, Y. Li, Z. Liang, Z. Bao, Y. Cui, *J. Am. Chem. Soc.* **2017**, *139*, 11550-11558.
[64] A. L. Michan, B. S. Parimalam, M. Leskes, R. N. Kerber, T. Yoon, C. P. Grey, B. L. Lucht, *Chem. Mater.* **2016**, *28*, 8149-8159.
[65] U. v. Alpen, *J. Solid State Chem.* **1979**, *29*, 379-392.
[66] F. A. Soto, Y. Ma, J. M. Martinez de la Hoz, J. M. Seminario, P. B. Balbuena, *Chem. Mater.* **2015**, *27*, 7990-8000.
[67] S. Shi, Y. Qi, H. Li, L. G. Hector, *J. Phys. Chem. C* **2013**, *117*, 8579-8593.
[68] J. M. Garcia-Lastra, J. S. G. Myrdal, R. Christensen, K. S. Thygesen, T. Vegge, *J. Phys. Chem. C* **2013**, *117*, 5568-5577.

Entry for the Table of Contents

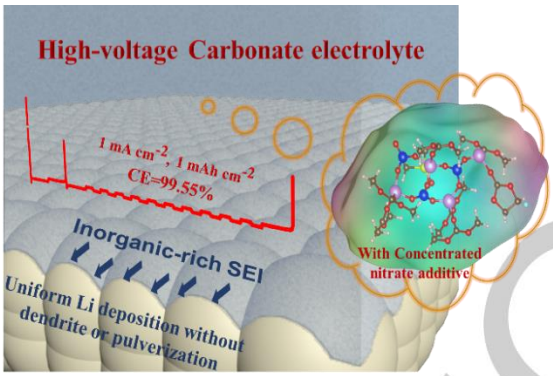

Based on density functional theory (DFT) calculation and experimental results, the inorganic-rich SEI has been constructed on Li metal to promote dense Li growth with a recorded Coulombic efficiency (CE) of 99.55% in the carbonate electrolyte. Such an outstanding SEI is in-situ synthesized on the surface of Li metal anode through using concentrated $LiNO_3$ in dimethyl sulfoxide (DMSO) as electrolyte additive in the FEC-based electrolyte, which has participated in the primary Li^+ solvation sheath with the aggregates structure and thus promote the preferential reduction of NO_3^- ions to form the inorganic-rich SEI.